High Velocity Perforation as a Benchmark Problem for Material Model Validation

Vladislav V. Vershinin

Department of Structural Mechanics, Moscow State University of Civil Engineering, 26 Yaroslavskoe shosse, Moscow 129337, Russia

Abstract: *High velocity perforation problem is taken as a benchmark to validate material plasticity and fracture models. 2024-T3(51) aluminum alloy is chosen as a reference material. Numerical simulations of a plate perforation using Johnson-Cook plasticity model with two sets of parameters, Johnson-Cook fracture criterion with one set of fitting parameters and pressure and Lode dependent ductile fracture criterion with three sets of material constants are performed into Abaqus/Explicit. Calibration of all the material constants is accomplished using results of quasi-static and high strain rate experiments. Problem formulation, plasticity and fracture models and their parameters, heating effects and friction are estimated independently in the context of their effect on the accuracy of the numerical solution. Ballistic limit velocity and residual velocity tests are employed for validation procedure. For one of the considered problem-models combination quantitative agreement with maximum discrepancy of less than 10% and good and physically sound qualitative correlation with the experimental results were obtained.*

Keywords: *Plasticity model, fracture criterion, plate perforation, numerical simulation.*

1. Introduction

Utilization of appropriate plasticity and fracture models in numerical simulation of various processes followed by large deformation and fracture of a material is of paramount significance for an accurate prediction of major qualitative and quantitative characteristics. High velocity perforation of metal plates is among such problems. The perforation process is characterized by high rate deformation and fracture. Stress states of the projectile and target materials are time-variant and complex, while failure mechanisms of the interacting bodies are dependent on their geometry and mechanical properties. That's why ballistic behavior of plates made of a particular material can be successfully used as a benchmark problem for validation of this material plasticity and fracture models.

Metal behavior has been extensively investigated for more than a century. Dozens of metal plasticity and fracture models have been developed, however open questions are still present that is proved by ongoing theoretical research. Plastic behavior of particular alloys is anisotropic (mainly in thin sheets) as well as dependent on pressure and the third invariant of the stress deviator (e.g., Barlat et al., 1991; Karafillis and Boyce, 1993; Brünig, 1999; Kroon and Faleskog, 2013; Cazacu and Barlat, 2004; Bai and Wierzbicki, 2008; Seidt and Gilat, 2013), so that it is necessary to employ newly developed elaborate plasticity models for a careful prediction of yielding of such materials. Fracture behavior of some metals is also rather complex, sometimes exerting dependence on stress tensor invariants (see Bai and Wierzbicki, 2008, 2010; Khan and Liu, 2012; Oyane et al., 1980; Johnson and Cook, 1985; Lou et al., 2013, 2014) and coupling with plastic behavior in the sense of its influence on strength of metals (Gurson, 1977; Tvergaard and

Needleman, 1984; Kachanov, 1958; Lemaitre, 1985; Chaboche, 1988a, 1988b; Brünig and Gerke, 2011). However, due to a comparatively large number of independent experimental tests necessary to calibrate elaborate models simple plasticity models and fracture criteria are still popular.

In the present paper plate perforation by a rigid spherical projectile is considered as a benchmark problem. As a calibrated and validated material 2024-T3(51) aluminum alloy is chosen. In the first part of the article results of the experiments conducted by the author are combined with the data available in literature and presented as a reference solution for the considered problem. In the second part of the work a description of the employed plasticity and fracture models, their parameters calibration procedure and results of numerical simulation utilizing these models are presented. During the numerical simulation problem formulation, heating effects, friction, elaboration and parameters of plasticity and fracture models are assessed independently in the sense of their influence on the qualitative and quantitative accuracy of modeling.

2. Benchmark problem description

As a benchmark problem for validation material plasticity and fracture models it was decided to consider plate perforation test with residual and ballistic limit velocities taken as reference parameters. One of the best alternatives for being considered as a benchmark material was 2024-T3(51) aluminum alloy, since large amount of experimental data and calibrated models of this material are available in literature. Evidently, plate perforation by a rigid projectile should be considered, so the simplest variant of this problem was chosen - circular 2024-T3(51) aluminum alloy plates normally impacted at the center by a rigid spherical projectile.

It was shown in (Vershinin, 2015) that for circular 2024-T3(51) aluminum alloy plates with normalized thicknesses $H/D \geq 0.19$, where H is the plate thickness and D is the projectile diameter, ballistic limit velocity V_{bl} (in $\mathrm{m/s}$) follows an empirical relation of the form

$$V_{\mathrm{bl}} = 622 \cdot \left(H/D\right)^{0.673} - 33 \qquad (2.1)$$

This relation was obtained from combination of the published results (Senf and Weimann, 1973) and new experimental data. In the new set of experiments free circular 2024-T3(51) aluminum alloy plates with a diameter $d = 81.4\ \mathrm{mm}$ and thicknesses in the range of $H = 0.9 \div 12.2\ \mathrm{mm}$ were used. Spherical projectiles with a diameter $D = 10.0\ \mathrm{mm}$ were made of AISI 52100 alloy steel. The V_{bl} values were determined as a half-sum of the lowest projectile velocity at which the plate perforation occurred and the highest projectile velocity at which a hard steel sphere did not perforate the plate. Additional details on the experiments can be found in (Vershinin, 2015).

It should be mentioned, that 2024-T3(51) aluminum alloy exerts no scale effects (Weimann, 1974) and boundary conditions have almost negligible influence on the V_{bl} values for $d/D > 8$ (Bivin, 2008, 2011). At the same time Eq. (2.1) is limited from above by cavitation phenomenon and should be used very carefully for velocities greater than 1000 $\mathrm{m/s}$.

3. Plasticity and fracture models. Implementation into Abaqus/Explicit

During numerical simulation the steel spherical projectile was modeled as elastic solid and the aluminum target plate – as destructible elastic-plastic solid. Plasticity and fracture models utilized for modeling of 2024-T3(51) aluminum alloy and implemented into Abaqus/Explicit are described below. They are Johnson-Cook plasticity model (Johnson and Cook, 1983) and two phenomenological fracture models – Johnson-Cook fracture criterion (Johnson and Cook, 1985) and ductile fracture criterion with pressure and Lode dependence (Lou et al., 2014), which is implemented into Abaqus/Explicit in a tabular form.

3.1. Johnson-Cook plasticity model

It was reported by many authors (see, for example, Barlat et al., 1991; Bai and Wierzbicki, 2008; Seidt and Gilat, 2013), that 2024-T3(51) aluminum alloy is not isotropic and for careful modeling of its behavior anisotropic and/or pressure and Lode angle parameter dependent yield functions must be utilized. However, some authors (e.g., Lesuer, 2000) claimed, that stress-strain behavior of the 2024-T3(51) alloy is isotropic and insensitive to mean stress. This statement was supported (Lesuer, 2000) by compression and tension tests on a split Hopkinson pressure bar using samples made from 4-mm thick plates. Stress-strain curves obtained in compression for the in-plane 0° (rolling direction), in-plane 90° and normal (through the thickness) orientations almost coincided (maximum deviation was 20 MPa). Material response in tension and compression under large-scale plastic flow was also indistinguishable. So, it was decided to try Johnson-Cook plasticity model (Johnson and Cook, 1983) at first. The choice was motivated by relative simplicity of the model, its widespread use and because it was already implemented into Abaqus/Explicit. As it will be shown below, the choice justified itself.

The Johnson-Cook plasticity model is based on the von Mises yield surface with the associated flow rule. According to this model, isotropic hardening law depends on the strain rate and temperature rise and has the following form:

$$\bar{\sigma} = \left[A + B\bar{\varepsilon}_{pl}^{n}\right]\left[1 + C\ln\left(\dot{\bar{\varepsilon}}_{pl}/\dot{\bar{\varepsilon}}_{0}\right)\right]\left[1 - \left(\frac{T - T_0}{T_m - T_0}\right)^{q}\right] \qquad (3.1)$$

where $\bar{\sigma}$ is the von Mises stress, $\bar{\varepsilon}_{pl}$ is the equivalent plastic strain, $\dot{\bar{\varepsilon}}_{pl}$ and $\dot{\bar{\varepsilon}}_{0}$ are the current and reference strain rates, respectively, T_{m} is the melting temperature, T_0 is the transition temperature below which the material strength has no temperature dependence, and A, B, C, n, q are five material constants, which need to be calibrated from experiments. As it is seen from Eq. (3.1) effects of strain hardening, strain rate hardening and temperature softening are uncoupled.

Due to high strain rates the plate perforation process was assumed to be adiabatic, so that numerical analysis was performed including effects of adiabatic heating. The temperature increase ΔT owing to plastic work is calculated on each increment through solving at each integration point the following heat equation:

$$\dot{T} = \frac{\chi}{\rho c_V}\boldsymbol{\sigma} : \dot{\boldsymbol{\varepsilon}}_{pl} \qquad (3.2)$$

where ρ is the density, c_V is the specific heat at constant volume, χ is the ratio of plastic energy converted to heat, $\boldsymbol{\sigma}$ is the stress tensor and $\dot{\boldsymbol{\varepsilon}}_{pl}$ is the plastic strain rate tensor. Target material physical, elastic and thermal properties assigned for the numerical simulation are taken from (Lesuer, 2000; Teng and Wierzbicki, 2004) and presented in Table 1, and constants of the plasticity model (5.1) are taken from (Lesuer, 2000; Johnson and Cook, 1983) and given in Table 2. Stress-strain curves obtained for the two material constant sets, which are presented in Tables 1, 2 and indexed as “P-I” and “P-II”, on a single element subjected to uniaxial tension under isothermal and adiabatic conditions with $\dot{\bar{\varepsilon}}_{pl} = 1$ are shown in Fig. 1.

Table 1. Physical, elastic and thermal properties of 2024-T3(51) aluminum alloy

Index	ρ, $\mathrm{kg/m^3}$	E, GPa	ν	c_V, $\mathrm{J/(kg \cdot K)}$	χ	T_m, K	T_0, K
P-I	2770	74.66	0.3	875	0.9	775	293
P-II	2770	74.66	0.3	875	0.9	775	293

Table 2. Constants of the Johnson-Cook plasticity model for AA2024-T3(51)

Index	A, MPa	B, MPa	n	C	q	$\dot{\bar{\varepsilon}}_0$, $\mathrm{s^{-1}}$
P-I	369	684	0.73	0.0083	1.7	1.0
P-II	265	426	0.34	0.0083	1.7	1.0

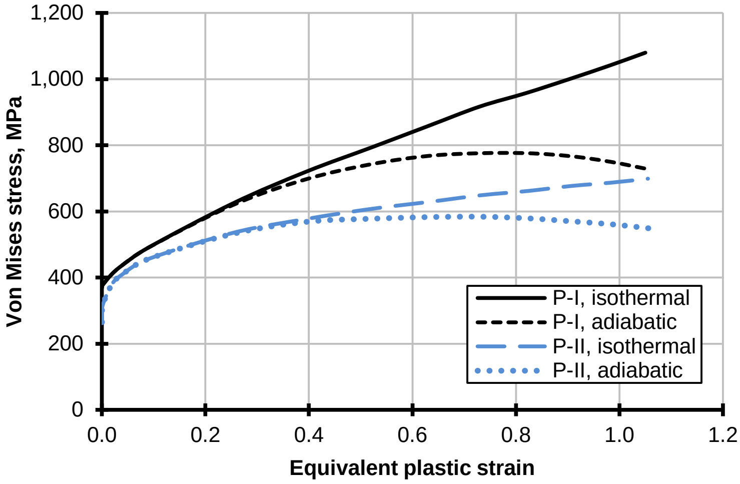

Fig. 1. Stress-strain curves obtained in Abaqus/Explicit for the two material constant sets on a single element subjected to uniaxial tension under isothermal and adiabatic conditions with $\dot{\bar{\varepsilon}}_{pl} = 1$

3.2. Johnson-Cook fracture model

The Johnson-Cook failure model is based on the value of the equivalent plastic strain at element integration points. The damage parameter is defined as

$$\omega = \sum \left(\Delta\bar{\varepsilon}_{pl} / \bar{\varepsilon}_{pl}^{f} \right) \qquad (3.3)$$

where $\Delta\bar{\varepsilon}_{pl}$ is an increment of the equivalent plastic strain, $\bar{\varepsilon}_{pl}^{f}$ is the equivalent plastic strain at failure, and the summation is performed over all increments in the analysis. When $\omega \geq 1$ failure is assumed to occur. An expression for the equivalent plastic strain at failure $\bar{\varepsilon}_{pl}^{f}$ which is used in Abaqus/Explicit slightly differs from the original formula (Johnson and Cook, 1985) and has the following form:

$$\bar{\varepsilon}_{pl}^{f} = \left[D_1 + D_2 \exp\left(D_3 \frac{p}{q} \right) \right] \left[1 + D_4 \ln\left(\frac{\dot{\bar{\varepsilon}}_{pl}}{\dot{\varepsilon}_0} \right) \right] \left[1 + D_5 \left(\frac{T - T_0}{T_m - T_0} \right) \right] \qquad (3.4)$$

Here $p = -\sigma_m = -\frac{1}{3}\mathrm{trace}(\boldsymbol{\sigma})$ is the pressure stress, $q = \bar{\sigma} = \sqrt{\frac{3}{2}(\mathbf{S}:\mathbf{S})}$, where $\mathbf{S} = \boldsymbol{\sigma} + p\mathbf{I}$ is the deviatoric stress, $D_1 - D_5$ are five material constants, which need to be calibrated from experiments, and the other variables were defined earlier in the text (see Subsection 3.1). Eq. (3.4) differs from the original formula in the sign of the parameter D_3. Values of the failure parameters $D_1 - D_5$ are taken from (Kay, 2003) and presented in Table 3. Thermal properties are identical to those used in the Johnson-Cook plasticity model (see Table 1).

Table 3. Parameters of the Johnson-Cook failure model for AA2024-T3(51)

Index	D_1	D_2	D_3	D_4	D_5	$\dot{\varepsilon}_0$, s^{-1}
JC	0.112	0.123	1.5	0.007	0.0	1.0

3.3. Ductile fracture criterion with pressure and Lode dependence

In Abaqus/Explicit the ductile fracture criterion may be defined in a tabular form as a function of equivalent plastic strain rate $\dot{\bar{\varepsilon}}_{pl}$, stress triaxiality $\eta = -p/q$, and the normalized third deviatoric stress invariant $\xi = (r/q)^3 = \cos(3\theta)$, where $r = \left[27\det(\mathbf{S})/2\right]^{1/3}$ is the third invariant of deviatoric stress and θ is the Lode angle. The function $\xi(\theta)$ can take values from $\xi = -1$, for stress states on the compressive meridian, to $\xi = 1$, for stress states on the tensile meridian. Damage accumulation and failure occur in the same manner, as in the Johnson-Cook fracture model (see Subsection 3.2).

To obtain values of equivalent plastic strain at failure $\bar{\varepsilon}_{pl}^{f}$ for different stress states a newly developed fracture model (Lou et al., 2014) was used. The proposed ductile fracture criterion has the form

$$\left(\frac{2}{\sqrt{L^2+3}} \right)^{C_1} \left(\frac{1}{1+C} \left[\eta + \frac{3-L}{3\sqrt{L^2+3}} + C \right] \right)^{C_2} \bar{\varepsilon}_{pl}^{f} = C_3 \qquad (3.5)$$

Here C_1, C_2, C_3 are three material constants to be calibrated from experiments, $L = \left(3\tan(\theta) - \sqrt{3}\right) / \left(\tan(\theta) + \sqrt{3}\right)$ is the Lode parameter which is related to the normalized third deviatoric stress invariant ξ in the following way:

$$\xi = -L\left(9 - L^2\right) / \left(L^2 + 3\right)^{3/2} \qquad (3.6)$$

Parameter $C = -\sigma_1/\bar{\sigma}$ represents the sensitivity of the cut-off value for the stress triaxiality to microscopic structure of a material. By the cut-off value the stress triaxiality below which fracture will never occur is meant. The Lode dependent cut-off value for the stress triaxiality is proposed to take a form of

$$\eta + \frac{3-L}{3\sqrt{L^2+3}} + C = 0 \qquad (3.7)$$

To calibrate the parameters $C_1,\ C_2,\ C_3$ experimental data (Bao, 2003; Seidt, 2010) was used. Values of stress state variables and equivalent plastic strain at failure $\bar{\varepsilon}_{pl}^{f}$ from these two experiment sets are presented in Table 4. It should be emphasized, that because of the fact that stress state parameters (η, ξ, L) are varying in the loading process, average values of these parameters were used. That's why three additional tests available (Khan and Liu, 2012) were not included in the data set – the authors reported only values of the stress state parameters at failure. The subscript "av" will be dropped and (η, ξ, L) will be understood as the average values, unless otherwise stated. Stress state parameters from the experiments (Bao, 2003; Seidt, 2010) along with the cut-off surfaces for the stress triaxiality (see Eq. (3.7)) at three different values of the parameter C are shown in Fig. 2.

Table 4. Equivalent plastic strains at failure and corresponding stress state parameters for 2024-T3(51) aluminum alloy

Test #	**Ref.**	$\bar{\varepsilon}_{pl}^{f}$	η	ξ	L
1	[93]	0.170	0.9300	1.000	-1.0000
2	[93]	0.210	0.6100	0.097	-0.0561
3	[93]	0.210	0.0124	0.055	-0.0318
4	[93]	0.260	0.1170	0.500	-0.3054
5	[93]	0.280	0.6300	1.000	-1.0000
6	[93]	0.310	0.3430	1.000	-1.0000
7	[93]	0.330	0.3560	0.984	-0.8666
8	[93]	0.341	-0.2240	-0.800	0.5531
9	[93]	0.356	-0.2330	-0.820	0.5749
10	[93]	0.360	0.3690	1.000	-1.0000
11	[93]	0.380	-0.2340	-0.810	0.5638
12	[93]	0.450	-0.2780	-0.910	0.6940
13	[93]	0.460	0.4000	1.000	-1.0000
14	[93]	0.480	0.3570	0.979	-0.8477
15	[93]	0.620	-0.2480	-0.840	0.5980
16	[94]	0.1036	0.5802	-0.0383	0.0221
17	[94]	0.1675	0.0006	0.0012	-0.0007
18	[94]	0.1951	0.5648	0.1474	-0.0855
19	[94]	0.1951	0.6052	0.2072	-0.1207
20	[94]	0.2017	0.7304	0.1085	-0.0628
21	[94]	0.2022	0.8556	1.0000	-1.0000
22	[94]	0.2160	0.2663	0.9336	-0.7352
23	[94]	0.2204	0.4974	0.6478	-0.4145
24	[94]	0.2419	0.4781	0.1896	-0.1103
25	[94]	0.2441	0.4319	0.8881	-0.6607
26	[94]	0.2447	0.7631	1.0000	-1.0000
27	[94]	0.2562	0.3376	0.9993	-0.9710
28	[94]	0.2656	0.1585	0.6581	-0.4228
29	[94]	0.2727	0.6765	1.0000	-1.0000
30	[94]	0.2832	0.5994	-0.4417	0.2662
31	[94]	0.2909	0.6072	1.0000	-1.0000
32	[94]	0.3080	0.5243	1.0000	-1.0000
33	[94]	0.3190	0.5994	-0.5180	0.3179
34	[94]	0.3224	0.3491	1.0000	-1.0000
35	[94]	0.5152	-0.1574	-0.6538	0.4193

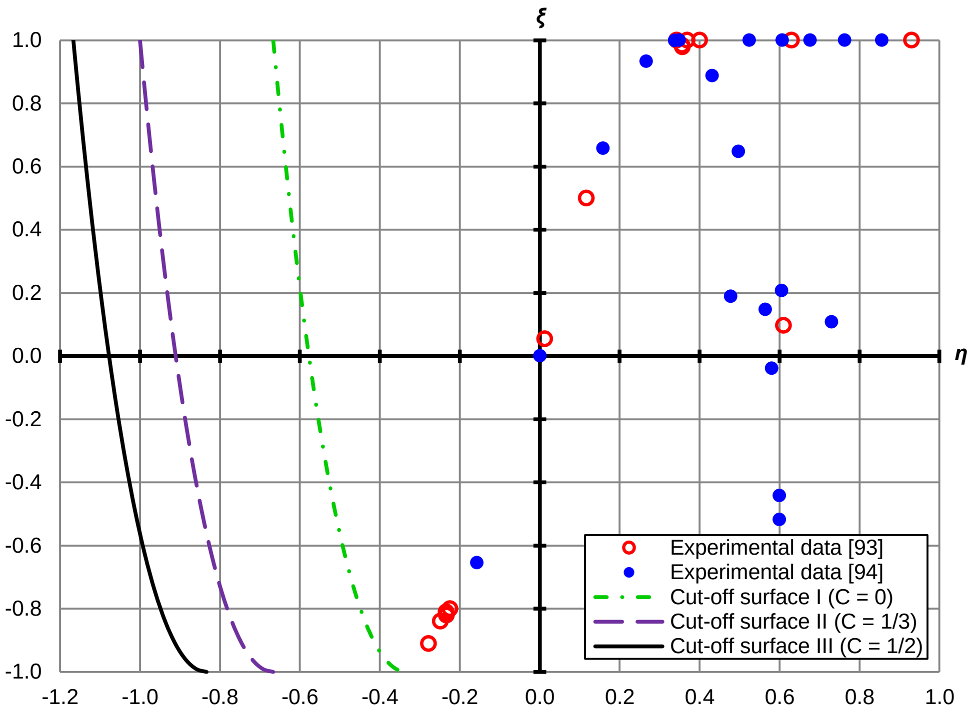

Fig. 2. Stress state parameters at failure and cut-off surfaces for the stress triaxiality (see Eq. (3.7)) for 2024-T3(51) aluminum alloy

Calibration of the parameters C_1, C_2, C_3 at three different values of the parameter C was performed using MATLAB Curve Fitting tool. The results of the calibration procedure are presented in Table 5.

Table 5. Calibrated material constants of the ductile fracture criterion for 2024-T3(51) aluminum alloy

Index	C	C_1	C_2	C_3
L-I	0	2.413	0.2762	0.2991
L-II	1/3	2.628	0.4879	0.3062
L-III	1/2	2.694	0.5842	0.3089

4. Results of numerical simulation

The numerical simulation was performed in both axisymmetric and 3-dimensional formulations (indexed “AX” and “3D”, respectively). The projectile impacted the target at its center; dimensions of the target and the projectile were equal to corresponding dimensions of the projectile and the target plates used in the experiments performed (see Section 2). In all cases, except those in which influence of friction was estimated, frictional coefficient was assumed to be equal to 0.2. Steel properties defined were the following: Young’s modulus $E = 210\ \text{GPa}$, Poisson’s ratio $\nu = 0.3$, density $\rho = 7830\ \text{kg}/\text{m}^3$.

As it is known processes followed by material fracture are irregular. However, analysis of the tests conducted as well as other available experimental results (e.g., Wingrove, 1973; Borvik et al., 2002) reveals that perforation of plates by rigid spherical nosed axisymmetric projectiles, which occurs through both shear plugging and ductile hole enlargement, can be considered as axisymmetric. So, it was decided, that axisymmetric problem formulation could also be employed (at least for targets with H/D ≥ 0.4, whose mechanisms of failure correspond to the mentioned above). It is realized by the author, that perforation of thin plates followed by petalling is strictly unsymmetrical process, but to complete the set axisymmetric formulation was applied to the whole range of the normalized thicknesses considered.

In the first set of the numerical tests $V_{\rm bl}$ values for different combinations of problem formulation and plasticity and fracture models were determined. The $V_{\rm bl}$ values obtained are presented in Table 6, while a disagreement of the numerical results with the experimental data (Vershinin, 2015) is shown in Fig. 3.

Table 6. Comparison of $V_{\rm bl}$ values obtained numerically with the experimental data

H/D	0.1	0.2	0.3	0.6	1.2	2.0
Experiment	138.3	177.6	243.6	408.0	670.2	958.7
AX/P-I/JC	109.5±0.5	175.5±0.5	235.5±0.5	361.5±0.5	571.5±0.5	924.5±0.5
3D/P-I/JC	91.5±0.5	154.5±0.5	236.5±0.5	382.5±0.5	542.5±0.5	934.5±0.5
3D/P-I/L-I	97.0±2.0	167.5±2.5	239.5±2.5	345.0±1.0	670.0±1.0	995.0±5.0
3D/P-I/L-II	96.5±0.5	164.0±1.0	226.5±2.5	361.0±1.0	653.0±3.0	982.0±2.0
3D/P-I/L-III	96.5±0.5	169.0±1.0	223.0±1.0	369.5±0.5	639.0±1.0	977.0±1.0
AX/P-I/L-III	114.0±1.0	187.0±1.0	241.0±1.0	349.0±1.0	637.0±1.0	977.5±2.5
3D/P-II/L-III	93.0±1.0	157.0±2.5	213.0±3.0	336.0±1.0	597.0±3.0	922.5±2.5

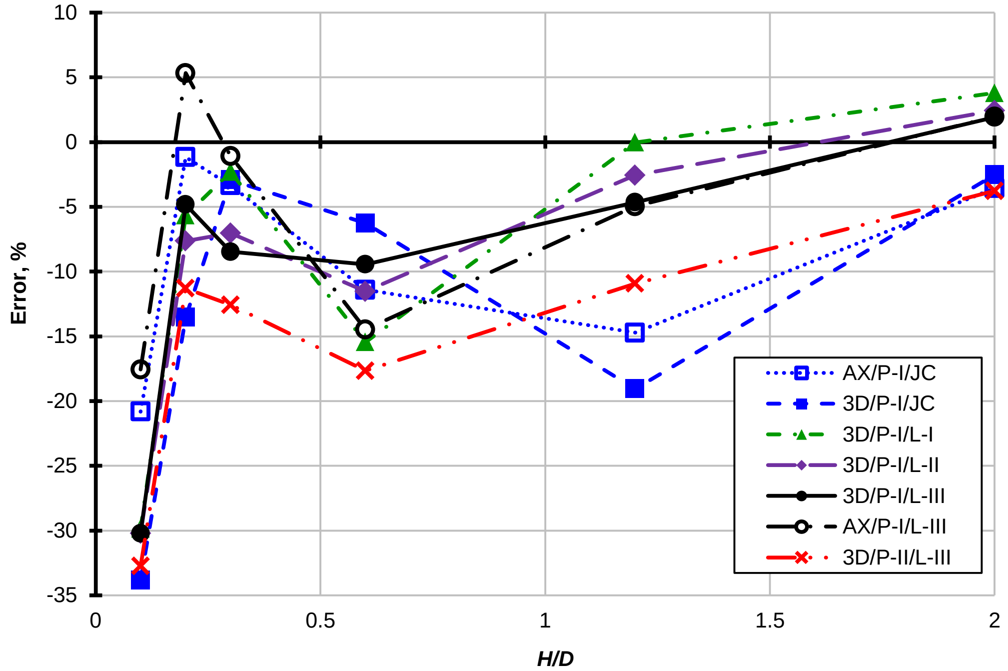

Fig. 3. Discrepancy between the numerical and experimental results (see Table 6)

It is clearly seen, that neither of the formulation-models combinations tested catches performance of thin plates with $H/D < 0.15$. Since two different yield surfaces were tested (cases “3D/P-I/L-III” and “3D/P-II/L-III”) and stress state of the target in the contact area changes with H/D increase, the most likely cause of such a discrepancy is that the fracture locus is poorly defined in some area in the $\eta - \xi$ plane. And there is a ring of truth about it, because, despite their large amount, experimental data on fracture of 2024-T3(51) aluminum alloy, which were used for the fracture locus calibration, are mostly concentrated in the first quadrant (see Fig. 2).

Meanwhile, compared with the experimental results, which follow Eq. (2.1), i.e. plates with $H/D \geq 0.19$, the error of the numerical results obtained using the “3D/P-I/L-III” formulation-models combination does not exceed 10%. And not only the quantitative agreement, but also good qualitative correlation of this formulation-models combination with the experiment was achieved. Views of plates of various thicknesses H/D after their perforation by a rigid spherical body with velocity nearly V_{bl} are presented in Fig. 4, and in Table 7 dimensions of the ejected plugs for H/D in the range 0.1–2.0 are compared with the values obtained experimentally. In Fig. 5 temperature field in the contact area of the $H/D = 1.2$ plate during its perforation is shown along with view of the corresponding test specimen after impact. Molten metal, which leads to the “snow cap” appearance on the projectile, and development of the “dead zone” are clearly seen. It is also remarkable, that for plates with $H/D \geq 0.19$ all of the problem-models combinations tested were within 20% of the experimental results.

Of course, there is certain dissimilarity in the numerical results and experimental data. The most pronounced take place for the cases, in which relative errors in V_{bl} determination are the largest. That is plates with $H/D = 0.3$ and $H/D = 0.6$. In both cases it is lack of ductility and fracture locus poorly defined in some area of the $\eta - \xi$ plane, which causes a discrepancy with the experiment.

In the target with $H/D = 0.3$ petals formed eventually break off. It should be mentioned, that petals break off actually takes place at higher projectile velocity, so that this phenomenon in the numerical simulation is just an early development of a really existing failure mechanism. As for the plate with *H/D* = 0.6, projectile passage through the hole, formed in the target after the plug ejection, varies in the numerical simulation and in the tests. As it is shown in Table 7, the plug diameter is smaller than the projectile diameter. So, in the experiment the projectile pushes the target material to the side (through ductile hole enlargement mechanism), when passing through the target. In the numerical simulation, in contrast, target material on the whole inner surface is just eroded. This yields lower resistance to perforation and underestimation of the ballistic limit. Also it should be noticed, that no developed spalling on the front side of thick plates, as it takes place in the experiment (Vershinin, 2015), was obtained in the numerical simulation.

Table 7. Dimensions of the ejected plugs. Comparison with the experiment

H/D	0.1	0.2	0.3	0.6	1.2	2.0
h_{plug}, Experiment	No plug	0.91*H*	0.87*H*	0.68*H*	0.49*H*	–
d_{plug}, Experiment	No plug	0.53*D*	0.80*D*	0.89*D*	1.13*D*	–
h_{plug}, 3D/P-I/L-III	0.87*H*	0.90*H*	0.86*H*	0.73*H*	0.49*H*	0.39*H*
d_{plug}, 3D/P-I/L-III	0.30*D*	0.54*D*	0.59*D*	0.73*D*	1.11*D*	1.11*D*

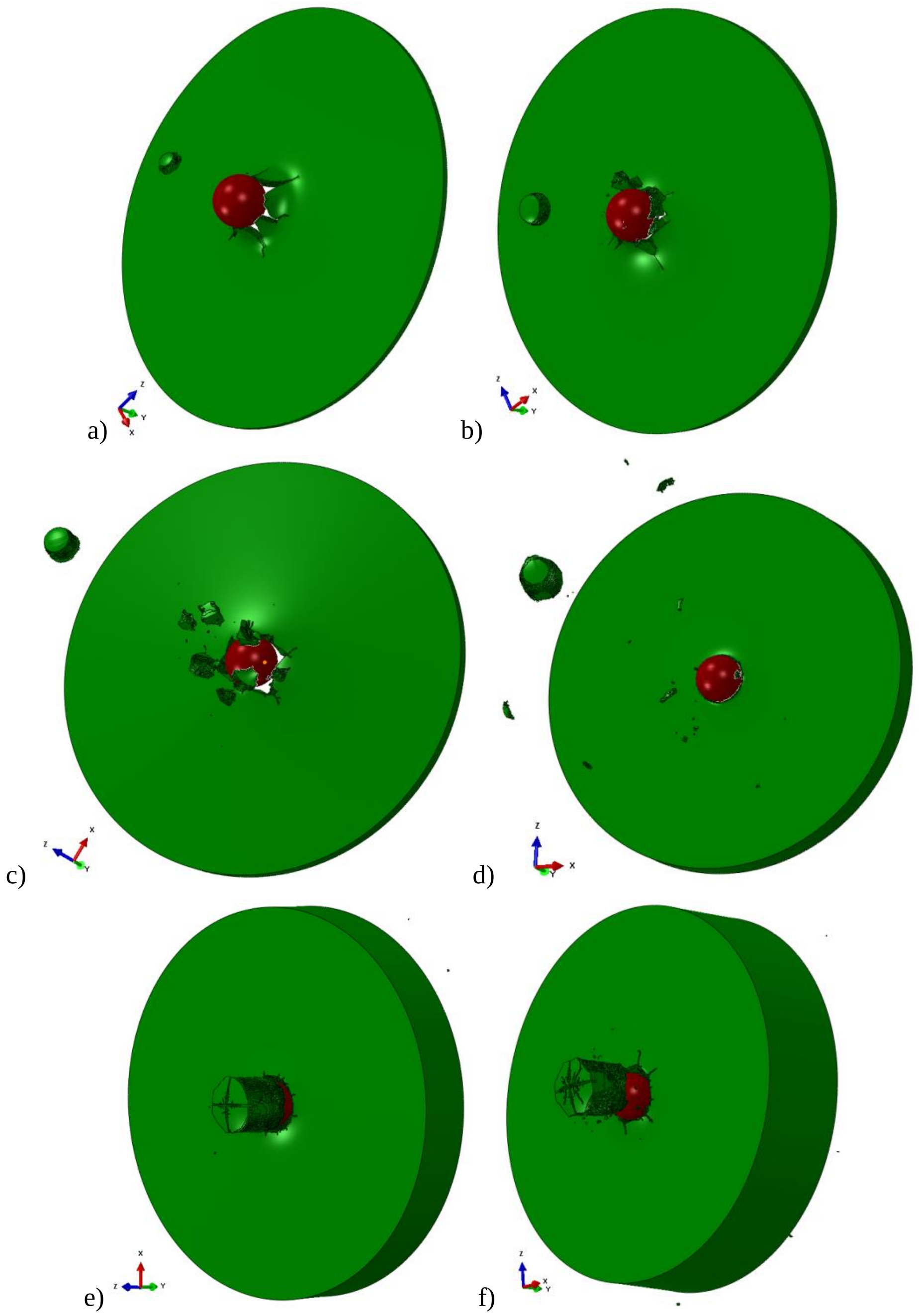

Fig. 4. Views of plates of various thicknesses H/D after their perforation by a rigid spherical body with velocity nearly V_{bl} : a) *H/D* = 0.1, V_0 = 97 m/s; b) *H/D* = 0.2, V_0 = 170 m/s; c) *H/D* = 0.3, V_0 = 224 m/s; d) *H/D* = 0.6, V_0 = 370 m/s; e) *H/D* = 1.2, V_0 = 640 m/s; f) *H/D* = 2.0, V_0 = 978 m/s

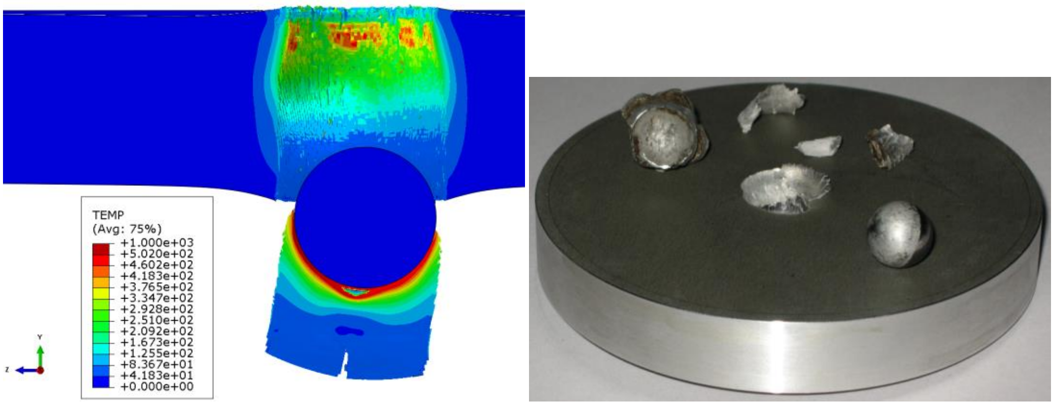

Fig. 5. Temperature field in $H/D = 1.2$ plate during its perforation with $V_0 = 640$ m/s and view of the corresponding test specimen after impact

In the second set of the numerical tests residual velocities V_r for plates of different thicknesses were determined using the best formulation-models combination “3D/P-I/L-III”. Normalized V_r versus V_0 data are compared with the experimental ones (Senf and Weimann, 1973) and shown in Fig. 6. Both numerical and experimental results scatter around a single curve, again confirming the validity of the utilized models.

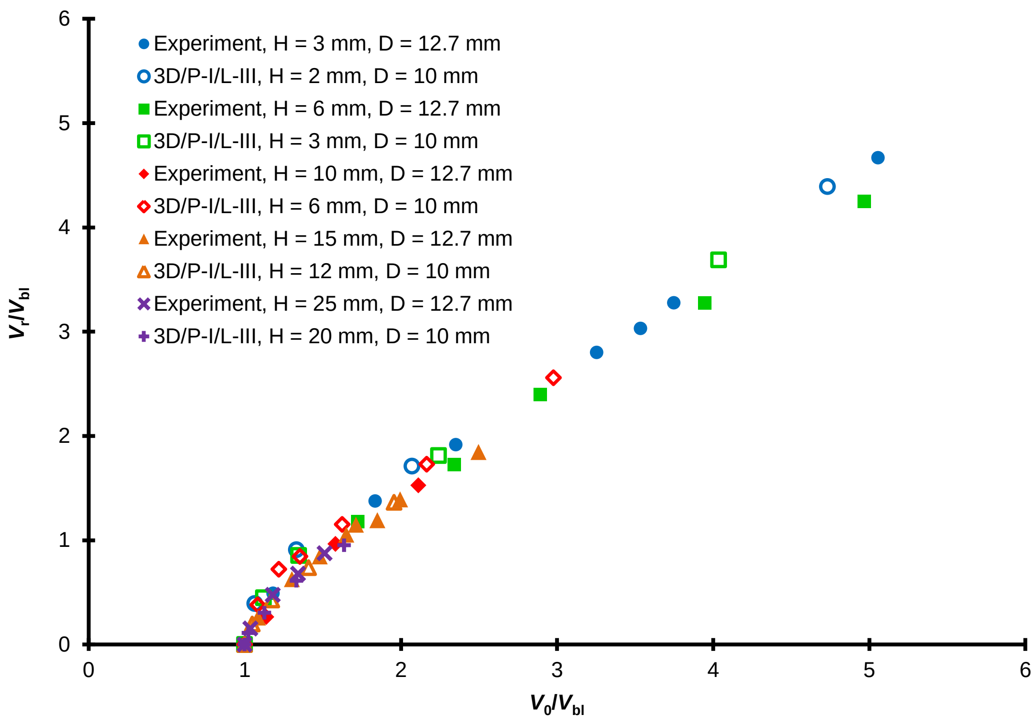

Fig. 6. Normalized residual projectile velocities. Comparison with the experiment

Finally, an effort to estimate influence of friction and heating effects was made. To accomplish this friction coefficient was, firstly, set equal to zero (no friction forces) and then to 0.47 (this value is usually considered as coefficient of kinematic friction for contact pair aluminum-steel). Results of numerical simulation of these cases are presented in Table 8 and indexed as “NF” (no friction) and “MF” (maximal friction), respectively. Also presented in Table 8 are results obtained numerically without any adiabatic heating effects and coefficient of friction set equal to 0.2. This data set is indexed as “NH” (no heating). All other material constants and problem formulation for these three extra cases were similar to those used in the “3D/P-I/L-III” formulation-models combination.

Table 8. Comparison of V_{bl} values obtained numerically for three extra cases with the experimental data

H/D	0.1	0.2	0.3	0.6	1.2	2.0
Experiment	138.3	177.6	243.6	408.0	670.2	958.7
3D/P-I/L-III	96.5±0.5	169.0±1.0	223.0±1.0	369.5±0.5	639.0±1.0	977.0±1.0
3D/P-I/L-III/NF	91.5±1.5	–	–	313.0±1.0	–	–
3D/P-I/L-III/MF	102.0±1.0	–	–	367.5±0.5	–	982.5±2.5
3D/P-I/L-III/NH	96.0±1.0	–	–	375.0±1.0	–	967.5±2.5

As is clearly seen form Table 8, influence of friction and heating effects on V_{bl} values is insignificant for the whole range of the target thicknesses considered. It should be only emphasized that setting friction coefficient equal to zero results in significant drop in target resistance to penetration, that is not consistent with the reality. This result may be considered as evidence of non-zero friction coefficient between a projectile and a target during high-velocity perforation despite high strain rates and melting.

5. Discussion and conclusions

Numerical simulations of circular 2024-T3(51) aluminum alloy plate perforation by a rigid spherical projectile were conducted in both axisymmetric and 3-dimensional formulations using Johnson-Cook plasticity model with two sets of fitting parameters, Johnson-Cook fracture criterion with one set of fitting parameters and pressure and Lode dependent ductile fracture criterion with three sets of material constants, which were implemented into Abaqus/Explicit code. It was found that valid plasticity and fracture models are of equal importance for an accurate modeling of high-rate, non-linear problems with material fracture, and disregarding of this fact can lead to a typical mistake (Seidt et al., 2013), that one can make. That is utilizing elaborate plasticity model and simple fracture criterion, or vice versa, that may result in a better agreement with the experimental results, but be physically wrong.

With all the formulation-models combinations employed the simulations were within 20% of the experimental results for the targets with $H/D \geq 0.19$. Moreover, with the Johnson-Cook plasticity model and the ductile fracture criterion with pressure and Lode dependence, which were calibrated using available experimental data, implemented into Abaqus/Explicit code and employed for 3-dimensional finite element analysis, quantitative agreement with maximum discrepancy less than 10% and good and physically sound qualitative correlation with the experimental results for circular 2024-T3(51) aluminum alloy plates with the normalized thicknesses $H/D \geq 0.19$ were obtained. These results confirmed the validity of the formulation-models combination employed and allow one to consider numerical simulation of high velocity perforation as an alternate way for validation of material plasticity and fracture models.

Influence of friction and heating effects appeared to be insignificant for projectile velocity up to $1000\ \mathrm{m/s}$, except the case when friction coefficient was set equal to zero, that resulted in significant drop in target resistance to penetration not consistent with the reality and revealed non-zero friction coefficient between a projectile and a target despite high strain rates and melting.

Acknowledgements

This work is a part of the research project financially supported by the Russian Foundation for Basic Research (project No. 14-08-00016).

References

1. Bai Y, Wierzbicki T. A New Model of Metal Plasticity and Fracture with Pressure and Lode Dependence. Int J Plast 2008;24(6):1071-96.
2. Bai Y, Wierzbicki T. Application of Extended Mohr-Coulomb Criterion to Ductile Fracture. Int J Fract 2010;161(1):1-20.
3. Bao Y. Prediction of Ductile Crack Formation in Uncracked Bodies. PhD Thesis. Cambridge, MA: Department of Ocean Engineering, Massachusetts Institute of Technology; 2003.
4. Barlat F, Lege DJ, Brem JC. A Six-Component Yield Function for Anisotropic Materials. Int J Plast 1991;7(7):693-712.
5. Bivin YK. Strain and Fracture of Circular Plates under Static and Dynamical Loading by a Spherical Body. Mech Solids 2008; 43(5): 798-807.
6. Bivin YK. Fracture of Circular Plates on Normal Impact by a Rigid Spherical Body. Mech Solids 2011; 46(4): 597-609.
7. Borvik T, Langseth M, Hopperstad OP, Malo KA. Perforation of 12 mm thick steel plates by 20 mm diameter projectiles with blunt, hemispherical and conical noses: Part I: Experimental study. Int J Imp Eng 2002;27(1):19-35.
8. Brünig M. Numerical Simulation of the Large Elastic-Plastic Deformation Behavior of Hydrostatic Stress-Sensitive Solids. Int J Plast 1999;15(11):1237-64.
9. Brünig M, Gerke S. Simulation of Damage Evolution in Ductile Metals Undergoing Dynamic Loading Conditions. Int J Plast 2011;27(10):1597-617.
10. Cazacu O, Barlat F. A Criterion for Description of Anisotropy and Yield Differential Effects in Pressure-Insensitive Metals. Int J Plast 2004;20(11):2027-45.
11. Chaboche JL. Continuum Damage Mechanics: Part I – General Concepts. J Appl Mech 1988;55(1):59-64.
12. Chaboche JL. Continuum Damage Mechanics: Part II – Damage Growth, Crack Initiation, and Crack Growth. J Appl Mech 1988;55(1):65-72.
13. Gurson AL. Continuum Theory of Ductile Rupture by Void Nucleation and Growth: Part I – Yield Criteria and Flow Rules for Porous Ductile Materials. J Eng Mater Technol 1977;99:2–15.
14. Johnson GR, Cook WH. A Constitutive Model and Data for Metals Subjected to Llarge Strains, High Stain Rates and Temperatures. In: Proceedings of the 7th International Symposium on Ballistics, Hague; 1983, p. 541-47.
15. Johnson GR, Cook WH. Fracture Characteristics of Three Metals Subjected to Various Strains, Strain Rates, Temperatures and Pressures. Eng Fract Mech 1985;21(1):31-48.

16. Kachanov LM. Time of the Rupture Process under Creep Conditions. Izvestiya Akademii Nauk SSSR. Otdelenie Technicheskikh Nauk 1958;8:26-31 (in Russian).
17. Karafillis AP, Boyce MC. A General Anisotropic Yield Criterion Using Bounds and a Transformation Weighting Tensor. J Mech Phys Solids 1993;41(12):1859-86.
18. Kay G. Failure Modeling of Titanium Ti-6Al-4V and Aluminum 2024-T3 with the Johnson-Cook Material Model. Technical Report DOT/FAA/AR-03/57. Livermore: Lawrence Livermore National Laboratory; 2003.
19. Khan AS, Liu H. A New Approach for Ductile Fracture Prediction on Al 2024-T351 Alloy. Int J Plast 2012;35:1-12.
20. Kroon M, Faleskog J. Numerical Implementation of a J_2- and J_3-Dependent Plasticity Model Based on a Spectral Decomposition of the Stress Deviator. Comput Mech 2013;52(5):1059-70.
21. Lemaitre J. A Continuous Damage Mechanics Model for Ductile Fracture. J Eng Mater Technol 1985;107(1):83-9.
22. Lesuer DR. Experimental Investigations of Material Model for Ti-6Al-4V Titanium and 2024-T3 Aluminum. Technical Report DOT/FAA/AR-00/25. Livermore: Lawrence Livermore National Laboratory; 2000.
23. Lou Y, Huh N, Lim S, Pack K. New Ductile Fracture Criterion for Prediction of Fracture Forming Limit Diagrams of Sheet Metals. Int J Sol Str 2012;49(25):3605-15.
24. Lou Y, Yoon JW, Huh H. Modeling of Shear Ductile Fracture Considering a Changeable Cut-Off Value for Stress Triaxiality. Int J Plast 2014;54:56-80.
25. Oyane M, Sato T, Okimoto K, Shima S. Criteria for Ductile Fracture and Their Applications. J Mech Work Tech 1980;4(1):65-81.
26. Seidt JD. Plastic Deformation and Ductile Fracture of 2024-T351 Aluminum under Various Loading Conditions. PhD Thesis. Columbus, OH: Department of Mechanical Engineering, The Ohio State University; 2010.
27. Seidt JD, Gilat A. Plastic Deformation of 2024-T351 Aluminum Plate under a Wide Range of Loading Conditions. Int J Sol Str 2013;50(10):1781-90.
28. Seidt JD, Pereira JM, Gilat A, Revilock DM, Nandwana K. Ballistic Impact of Anisotropic 2024 Aluminum Sheet and Plate. Int J Imp Eng 2013;62:27-34.
29. Senf H, Weimann K. Die Wirkung von Stahlkugeln auf Dural-Einfach-und Mehrplattenziele. EMI Report No. V6-73 (in German), 1973.
30. Teng X, Wierzbicki T. Effects of Fracture Criteria on High Velocity Perforation of Thin Beams. Int J Comput Meth 2004;1(1):171-200.
31. Tvergaard V, Needleman A. Analysis of the Cup-Cone Fracture in a Round Tensile Bar. Acta Metall 1984;32(1):157-69.
32. Vershinin VV. Validation of Metal Plasticity and Fracture Models through Numerical Simulation of High Velocity Perforation. Int J Sol Str 2015 (submitted).
33. Weimann K. Penetration of Steel Spheres in Aluminum Targets. EMI Report, E3/74 (in German), 1974.
34. Wingrove AL. The influence of projectile geometry on adiabatic shear and target failure. Metall Trans 1973;4(8)1829-33.